The Astrophysical Journal, 840:55 (11pp), 2017 May 1 https://doi.org/10.3847/1538-4357/aa6bf9

Radiative Transfer in a Translucent Cloud Illuminated by an Extended Background Source

Davide Biganzoli[1,2], Marco A. C. Potenza[2], and Massimo Robberto[3,4]
[1] Università degli Studi dell'Insubria Dept. of Science and High Technology Via Valleggio, 11, I-22100 Como, Italy
[2] Universitá degli Studi di Milano Dept. of Physics Via Celoria 16, I-20133 Milano, Italy
[3] Space Telescope Science Institute Baltimore, MD 21218, USA; robberto@stsci.edu
[4] Center for Astrophysical Studies Johns Hopkins University Baltimore, MD 21218, USA
Received 2016 October 7; revised 2017 April 4; accepted 2017 April 4; published 2017 May 4

Abstract

We discuss the radiative transfer theory for translucent clouds illuminated by an extended background source. First, we derive a rigorous solution based on the assumption that multiple scatterings produce an isotropic flux. Then we derive a more manageable analytic approximation showing that it nicely matches the results of the rigorous approach. To validate our model, we compare our predictions with accurate laboratory measurements for various types of well-characterized grains, including purely dielectric and strongly absorbing materials representative of astronomical icy and metallic grains, respectively, finding excellent agreement without the need to add free parameters. We use our model to explore the behavior of an astrophysical cloud illuminated by a diffuse source with dust grains having parameters typical of the classic ISM grains of Draine & Lee and protoplanetary disks, with an application to the dark silhouette disk 114–426 in Orion Nebula. We find that the scattering term modifies the transmitted radiation, both in terms of intensity (extinction) and shape (reddening) of the spectral distribution. In particular, for small optical thickness, our results show that scattering makes reddening almost negligible at visible wavelengths. Once the optical thickness increases enough and the probability of scattering events becomes close to or larger than 1, reddening becomes present but is appreciably modified with respect to the standard expression for line-of-sight absorption. Moreover, variations of the grain refractive index, in particular the amount of absorption, also play an important role in changing the shape of the spectral transmission curve, with dielectric grains showing the minimum amount of reddening.

Key words: dust, extinction – ISM: clouds – radiative transfer

1. Introduction

The increase in sensitivity, spatial resolution, and areal coverage of infrared instrumentation has recently enabled new detailed studies of translucent clouds, which are defined as clumps of interstellar material with optical depth in the range 1 to 5 at some observable wavelength (Van Dishoeck & Black 1986). The intermediate opacity of these systems produces measurable attenuation and reddening of background sources, without completely precluding their observation. If the background source density is high enough, or if the brightness of a diffuse background is uniform enough, it is possible to reconstruct the density profile of the cloud for an assumed reddening law. Density maps of translucent clouds have been obtained for a variety of systems, such as, e.g., the Bok globule Barnard 68 (Alves et al. 2001), the translucent clouds detected by *Spitzer* (Ingalls et al. 2011) and *Herschel* (Dunham et al. 2014), and the giant dark silhouette disk 114–426 in the Orion Nebula Cluster (Shuping et al. 2003; Miotello et al. 2012). Comparing density maps taken at different wavelengths allows us to derive the abundances of individual species (molecules, ices, dust grains) and their growth (Flagey et al. 2013).

The analysis of the these systems is normally carried out by applying the familiar expressions for the interstellar reddening toward a point source, i.e., the exponential decay law known as the Lambert–Beer–Bouguer (LBB) law. However, when the source of background illumination is extended and diffuse, analysis of the results may require some special attention from the point of view of radiative transfer. Let us take as an illustration the case of the giant dark silhouette disk 114–426 in the Orion Nebula. This source is close enough to the luminous backdrop of the Orion Nebula that an appropriate treatment of the radiative transfer through the outer parts of the disk must take into account the fact that each particle is illuminated by an extended, diffuse source. Extended illumination means that radiation propagating in every direction can be scattered toward the observer, thus partially compensating for the direct extinction along the line of sight. In cases like this, a one-dimensional treatment where there is only absorption along the line of sight may not be entirely adequate.

In this paper we develop a general, simplified treatment of the scattering by a cloud illuminated by extended, diffuse radiation. In Section 2 we present analytic solutions of the Radiative Transfer Equation (RTE) that can be used in a wide range of astrophysical conditions. In Section 3 we derive a simplified analytic expression to easily estimate the radiative transfer in the most interesting cases. In Section 4 we validate our models using an experimental apparatus specifically designed to reproduce an extended, diffuse, white light source, illuminating a sample cell containing water suspensions of well-known scatterers. In particular, we report the results obtained with calibrated, monodisperse polystyrene spheres at different concentrations and with polydisperse, nonspherical particles, representative of purely dielectric and strongly absorbing materials, respectively. Finally, in Section 5 we explore how the scattering terms affect the spectral intensity transmitted by a translucent cloud with typical astronomical grains, using grain mixtures appropriate for the ISM and young circumstellar disks, with an application to the 114–426 disk. The Appendix details the methods adopted to achieve absolute, independent characterization of our dust samples, a fundamental step for assessing the validity of our experimental results without tuning any free parameter.

2. Radiative Transfer Inside a Cloud

The general problem of describing the radiative transfer inside a cloud illuminated by an extended source emitting diffuse radiation has been solved analytically in several ways. Analytic solutions have been obtained assuming Rayleigh scattering (Plass et al. 1973), or making use of iterated integrals to compute Chandrasekhar's functions S and T (Chandrasekhar 1960), which give the transmitted and reflected radiation (e.g., Tanaka 2003, 2005). Similar problems have been addressed by Chandrasekhar himself, and solved later in several ways, as shown, for example, in Liuo (1973), Chalhoub (2005), and Barman (2000). The discrete ordinates method, in particular, gives a solution by expanding the phase function in Legendre polynomials. This approach is extremely powerful, but the analytic expression for the solution is very complex and difficult to handle. Other approaches make use of numerical solutions, e.g., Siewert (2000), Herman & Browning (1965), Jablonski (2012).

Here we introduce a simplified analytic model that can be conveniently used to describe light scattering from a cloud of randomly distributed particles illuminated by an extended source. Our goal is to obtain the radiation flux emerging in a given direction, to be detected at a very large distance from the cloud. We give a solution in terms of the typical quantities exploited in radiative transfer models: (1) the phase function $p(\theta)$, (2) the optical thickness of the system, τ, i.e., the length over which intensity is attenuated by a factor $1/e$; and the single-scattering albedo, $\omega = \frac{1}{4\pi}\int p(\theta)\sin\theta d\theta d\varphi$, the average of the phase function over the sphere. The way these parameters can be determined will be discussed below.

Let us start by recalling the general formulation of the RTE, in the form used to describe a monodimensional cloud of particles extended along the z axis, which also represents the line of sight of the observer. The RTE is generally written as

$$-\cos\theta\frac{dI}{d\theta} = \alpha I - \mathfrak{I}. \quad (1)$$

Here we follow the notation adopted in Chandrasekhar (1960), using I to indicate the light intensity (W m^{-2}) and $\mathfrak{I}$ to indicate the source term, here represented by the scattering events occurring within the cloud. The absorption coefficient, α, is the the product of the extinction cross-section, $C_{\rm ext}$ and the number density of particles, n, both related to the extinction-optical thickness, τ, by the expression $\tau = C_{\rm ext}nz$ where z is the geometrical thickness of the medium; finally, θ is the observation angle measured with respect to the z axis; if the observer is along the z axis it is $\theta = 0$.

To determine the radiation emerging from the cloud, one has to account for both the contribution of the transmitted light along the line of sight and that of the light redirected toward the observer by scattering events. While the former contribution can be described by the LBB law, the latter is generally more complex. In general, however, the scattered light toward the observer can be attributed (1) to single-scattering events, redirecting light entering the cloud from all directions, as well as (2) to the last of two or more scattering events. Before discussing these two effects, it is useful to make a couple of preliminary considerations, as they represent limit cases of our model.

First, we note that, thanks to the Principle of Reversibility of the optical path, for (a) a perfectly isotropic diffuse source surrounding the cloud, and for (b) pure dielectric particles (for which $\omega = 1$ rigorously), the probability of removing some radiation from the line of sight (due to scattering in any direction) is exactly the same as the probability that radiation is injected along the line of sight from any direction. The net result is no extinction at all. Of course, as soon as one of the two hypotheses is removed, this result is no longer valid: dropping (a) we find that light scattered toward a direction from which the source is not illuminating the cloud is not compensated, while dropping (b) the radiation is partially absorbed (and possibly re-emitted at other wavelengths). Our second simple consideration is that for an optically thick cloud composed of pure dielectric particles and illuminated by a source with any geometry, i.e., it is non-isotropic, the whole radiation power entering the cloud will be isotropically scattered.

In the real world the above assumptions are hardly valid, so the full RTE must be used. Our approach starts with the RTE formally expressed by Equation (1), writing a convenient approximation for the source term $\mathfrak{I}$ that accounts for all scattering events delivering light into the line of sight.

We assume that the cloud is a plane-parallel slab of translucent medium, with a finite optical thickness τ along the z direction and infinitely extended in the transversal plane. The radiation source is described by a uniform distribution of emitters, covering a given solid angle Ω, and with an energy spectral distribution $I(\nu)$. In Figure 1 we put it in the negative z hemisphere for simplicity, but the following arguments will not require this limitation.

Our expression for the source term $\mathfrak{I}$ in the RTE (Equation (1)) treats the single-scattering and multiple-scattering events differently. Single-scattering events can be described on the basis of the traditional scattering models for spheres (see, for example, Van de Hulst 1981), or any more refined numerical and/or analytic approach, e.g., Discrete Dipole Approximation (Purcell & Pennypacker 1973) or Finite Different Time Domain (Taflove et al. 1988). Following Chandrasekhar (1960), we adopt the single-scattering-phase functions. Multiple-scattering is described through the simplifying assumption that just two scattering events are enough to make the scattering isotropic. Multiple-scattering can thus be treated as isotropic scattering minus single-scattering, already accounted for in the first term. This approximation sets a limit to the reduced size of the scatterer, $\beta = ka = 2\pi a/\lambda$, where a represents the radius and λ is the radiation wavelength, as it is well satisfied for $\beta \ll 10$. A detailed discussion of this assumption, and the implications in an astrophysical context, will be presented in Section 4.2. Apart from this, we do not constrain the nature of the particles, which can be a collection of scatterers of any nature, size distribution, composition, shape, or internal structure.

Given the two phase functions p_s and p_m for the single- and multiple-scattering, the RTE can be expressed as follows

$$\begin{aligned} -\frac{dI}{d\tau} = {} & I_0 e^{-\tau} \\ & - \frac{1}{4\pi}\int_{4\pi} I_i(\tau, \mu', \varphi', \mu_0, \varphi_0) p_s(\mu', \varphi') d\mu' d\varphi' \\ & - \frac{1}{4\pi}\int_{4\pi} \tilde{I}_i(\tau, \mu'', \varphi'', \mu_0, \varphi_0) p_m(\mu'', \varphi'') d\mu'' d\varphi'' \end{aligned} \quad (2)$$

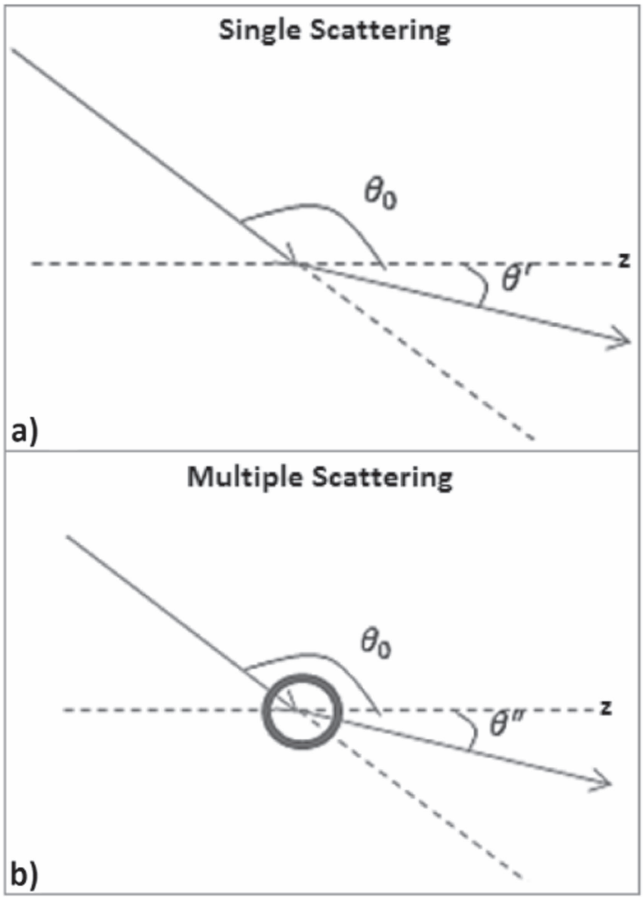

Figure 1. Schematic representation of the single (a) and multiple (b) scattering processes as considered in this work. In the case of single-scattering, the radiation comes from an angular direction θ_0 and it is deflected by an angle θ'. In the case of multiple-scattering, the radiation comes from an angular direction θ_0 and is deflected by the same angle as result of the last scattering event within the medium.

where the polar angles θ and ϕ have been introduced as described in Figure 1 and we have adopted the usual convention $\mu = \cos\theta$. The first term accounts for the photons injected along the line of sight from single-scattering events and the second term for the photons injected through multiple-scattering events.

The formal solution of Equation (2) takes a rather compact form:

$$I(\tau) = I_0 e^{-\tau} + \frac{I_0}{2}\int_\Omega \mu_0(1 - e^{-\tau/\mu_0})\int_{-1}^{+1} P(\mu_0, \mu') \times d\mu_0 d\mu'. \quad (3)$$

Here, Ω is the angular range subtended by the source, $I_0 = \int_\Omega I_i(\tau, \mu', \varphi', \mu_0, \varphi_0)d\Omega = \tilde{I}_i(\tau, \mu'', \varphi'', \mu_0, \varphi_0)$ and $P = p_s + p_m$, where $p_s = \frac{p(\theta)}{K}$ and $K = \int_{[0;\pi]} p(\theta)\sin\theta d\theta$.

To evaluate p_m, first we consider the fraction of light that is generally scattered, simply given by $1 - e^{-\tau/\mu_0}$ for a medium with optical thickness τ/μ_0. Then we need to subtract the probability of having only one scattering, obtained by integrating the phase function introduced above and taking into account the extinction of the incoming radiation along the direction μ_0. The phase function for the multiple-scattering is

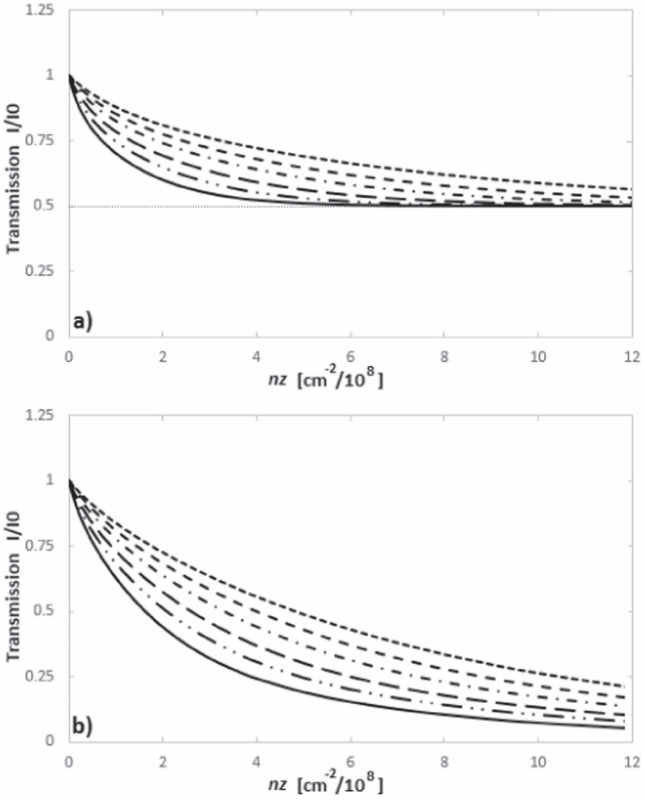

Figure 2. RTE solutions in terms of the transmission ratio for radiation coming from a semispace ($\Omega = 2\pi$ sr) for different wavelengths. From top to bottom: 900, 800, 700, 600, 500, and 400 nm. (a) Purely dielectric particles with a diameter of 0.6 μm and refractive index $n = 1.3$ in vacuum. (b) Absorbing particles with the same diameter and refractive index $n = 1.3 + i0.03$, giving rise to a scattering albedo $\omega_0 \approx 0.9$.

then:

$$p_m = 1 - e^{-\tau/\mu_0} - \frac{1}{2K}\int_\Omega\int_{-1}^{+1} \mu_0 p(\mu_0, \mu')(1 - e^{-\tau/\mu_0})d\mu_0 d\mu'. \quad (4)$$

To illustrate the results obtained from solution 3, we introduce the transmission as the ratio I/I_0.

In Figure 2(a) we plot an example of the transmission ratio as a function of the optical thickness (average value over all the wavelength range) of the cloud, in the ideal case of dielectric scatterers. We consider monodisperse (same size), spherical particles with a refractive index $n = 1.7$, and a diameter of 0.6 μm. The corresponding phase functions can be evaluated on the basis of the Mie expansions and the solution can be obtained by integrating over the semispace $\Omega = 2\pi$ sr subtended by the background source. In this case the source has been assumed to radiate as a blackbody at 3000 K. Different wavelengths are shown by different lines, as detailed in the legend. The asymptotic behavior for large optical thickness shows that half of the light is backscattered, and half is forward-scattered in the cloud, consistent with what is discussed above. In Figure 2(b) we show the results obtained by adding some absorption to the same particles, by adding an imaginary part $i0.03$ to the refractive index. The two cases are different mostly due to the presence of a horizontal asymptote at large optical thicknesses in the case of pure dielectric particles, which disappears in the case of absorption. This is again in accordance with what we mentioned earlier, invoking

the Principle of reversibility of the optical path: even at the highest optical thicknesses, when the cloud completely extinguishes the incoming radiation, scattering collects radiation from other directions and delivers it along the line of sight.

The asymptotic value of the extinction depends on the amplitude of the solid angle subtended by the source:

$$\lim_{\tau\to+\infty} I(\tau) = I_0 \int_D \mu_0 d\mu_0, \tag{5}$$

where D is the angular range of the azimuthal angle θ_0, and $\mu_0 = \cos\theta_0$. We have $D \subseteq [\pi/2, \pi]$. The transmission through the cloud is systematically higher than that in the case of a pointlike source, where the single LBB law gives $I(\tau)/I_0 = e^{-\tau}$.

In Figure 3 we plot the transmission ratio as a function of the optical thickness for different angular ranges D. We assume a source azimuthally symmetric around the direction of observation. Figure 3 shows that there are different horizontal asymptotes for different angular ranges. The solid line corresponds to the LBB law that gives the lowest transmission.

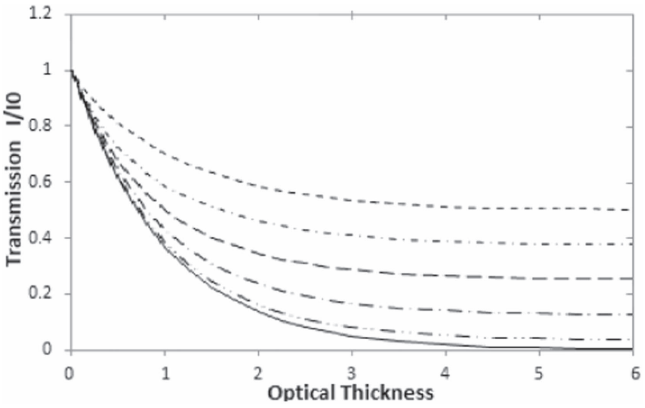

Figure 3. RTE solutions for different angles subtended by the source. From top to bottom the maximum illumination angles are 90°, 60°, 45°, 30°, 15°, and 0°. The LBB model (0) gives the lowest transmission.

3. A Simplified Analytic Solution

In this section we derive an analytic solution of the RTE introduced above (Equation (3)) by introducing a simplified expression for the phase functions. This solution, although approximated, can be used to evaluate the effect of the extended illumination from a few main parameters.

Lets start with the formal result for the general solutions of Equations (2) and (3). The general expression for $I(\tau)$ can be written as

$$\begin{aligned} I(\tau) = {} & I_0 e^{-\tau} + \frac{I_0}{2K}\int_D \int_{[0;\pi]} |\cos\theta_0|(1 - e^{-\tau/|\cos\theta_0|}) \\ & \times p(\theta_0;\, \theta')\sin\theta_0 \sin\theta' d\theta_0 d\theta' \\ & + I_0 \int_D |\cos\theta_0|\, e^{-\tau_A/|\cos\theta_0|}(1 - e^{-\tau_S/|\cos\theta_0|}) \\ & \times (1 - e^{-\tau/|\cos\theta_0|})\sin\theta_0 d\theta_0 \\ & - \frac{I_0}{2KV}\int_D |\cos\theta_0|(1 - e^{-\tau/|\cos\theta_0|})\sin\theta_0 d\theta_0 \\ & \cdot \int_D \int_{[0;\pi]} |\cos\theta_0|(1 - e^{-\tau/|\cos\theta_0|}) \\ & \times p(\theta_0;\, \theta')\sin\theta_0 \sin\theta' d\theta_0 d\theta' \\ = {} & I_0 e^{-\tau} + \frac{I_0}{2K}\Sigma(\tau) + I_0\chi(\tau) - \frac{I_0}{2KV}\Lambda(\tau)\Sigma(\tau), \end{aligned} \tag{6}$$

having indicated with $\Sigma(\tau)$, $\chi(\tau)$, and $\Lambda(\tau)$ the integrals in the equation. The main obstacle to the analytic integration is represented here by the phase function p. We therefore introduce a simplified expression describing the diffractive behavior of the angular intensity distribution for a particle of generic size, within a given range as discussed below. The following expression for the form factors of particles with size (diameter) d, so that the reduced size is $b = kd/2$, and $\beta = \frac{\pi}{b}$, exactly reproduces the zeroes of the typical diffraction patterns of objects with diameter d:

$$p(\tilde\theta) = \begin{cases} \dfrac{1 + \cos(b\tilde\theta)}{2}; & \tilde\theta \in [0;\, \beta] \\ 0; & \text{otherwise} \end{cases} \tag{7}$$

with $p(\beta) = 0$ for $\theta > \beta$. Note that this is just the first order of the typical expansion used for describing the phase functions (Chandrasekhar 1960).

The normalization factor K in Equation (6) thus becomes:

$$K = \omega \int_{[0;\pi]} p(\tilde\theta)\sin\tilde\theta d\tilde\theta = \omega\frac{\pi^2 - 2\beta^2 - \pi^2\cos\beta}{2(\pi^2 - \beta^2)}. \tag{8}$$

This expression is valid as long as the size of the particles is small enough that $\beta \gtrsim \frac{\pi}{6}$. This is in accordance with the limited validity of the assumption based upon the diffraction we make here to estimate the angular aperture of the diffracted intensity distribution. On the other hand, additionally, sizes much smaller than the wavelength are not described well here, since the diffraction approximation fails, and we can assume the scattered intensity to be isotropic just from the first scattering event. Nevertheless, the range of validity imposed by these arguments remains fully consistent with the aims of the model presented here, which is thought to be used for particles the size of the wavelength or slightly larger.

By inserting the phase function (7) in Equation (6), we obtain the following simplified expression:

$$\begin{aligned} \Sigma(\tau) = {} & \int_D \int_{[0;\pi]} |\cos\theta_0|(1 - e^{-\tau/|\cos\theta_0|})p(\theta_0;\, \theta')\sin\theta_0 \\ & \times \sin\theta' d\theta_0 d\theta' \\ = {} & \int_{[\pi-\delta,\pi]} \int_{[0;\pi]} |\cos\theta_0|(1 - e^{-\tau/|\cos\theta_0|})p(\theta_0;\, \theta') \\ & \times \sin\theta_0 \sin\theta' d\theta_0 d\theta' \\ = {} & \left| \int_{[0;\delta]} d\theta_0 \sin\theta_0 \cos\theta_0 (1 - e^{-\tau/\cos\theta_0}) \right. \\ & \left. \times \underbrace{\int_{[\theta_0;\theta_0+\beta]} \frac{1 + \cos[b(\theta' - \theta_0)]}{2} \sin\theta' d\theta'}_{\sigma(\theta_0)} \right| \\ = {} & \left| \int_{[0,\delta]} \sigma(\theta_0)\sin\theta_0\cos\theta_0(1 - e^{-\tau/\cos\theta_0}) d\theta_0 \right|, \end{aligned} \tag{9}$$

where $\pi - \delta$ is the minimum angle from which light is drawn toward the cloud, thus defining the illumination angular domain D.

The integral over θ_0 immediately gives:

$$\sigma(\theta_0) = \int_{[\theta_0;\theta_0+\beta]} \frac{1+\cos[b(\theta'-\theta_0)]}{2}\sin\theta' d\theta' = \frac{\pi^2 - 2\beta^2 - \pi^2\cos\beta}{2(\pi^2-\beta^2)}\cos\theta_0 + \frac{\pi^2\sin\beta}{2(\pi^2-\beta^2)}\sin\theta_0. \quad (10)$$

Equation (9) can therefore be expressed as the sum of two terms:

$$\Sigma_1(\tau) = \int_{[0;\delta]} (1 - e^{-\tau/\cos\theta_0})\sin\theta_0\cos^2\theta_0 d\theta_0, \quad (11)$$

$$\Sigma_2(\tau) = \int_{[0;\delta]} (1 - e^{-\tau/\cos\theta_0})\sin^2\theta_0\cos\theta_0 d\theta_0. \quad (12)$$

The first of these two functions cannot be integrated analytically, while the second admits a primitive. But we note that the two functions are almost identical, except for a scale factor that can be easily fixed by imposing the asymptotes for large τ to be equal. By evaluating the two asymptotic values analytically, we find:

$$L_1 = \lim_{\tau\to\infty}\Sigma_1(\tau) = \int_{[0;\delta]}\sin\theta_0\cos^2\theta_0 d\theta_0 = \frac{1-\cos^3\delta}{3}, \quad (13)$$

$$L_2 = \lim_{\tau\to\infty}\Sigma_2(\tau) = \int_{[0;\delta]}\sin^2\theta_0\cos\theta_0 d\theta_0 = \frac{\sin^3\delta}{3}. \quad (14)$$

We end up with a simple receipt to evaluate the function $\Sigma_1(\tau)$ through the analytic expression of $\Sigma_2(\tau)$. The integration gives:

$$\begin{aligned}\Sigma_1 = \frac{1}{6}[&\tau^3(\mathrm{Ei}(-\tau/\cos\delta) - \mathrm{Ei}(-\tau)) \\ &+ \tau^2(\cos\delta e^{-\tau/\cos\delta} - e^{-\tau}) \\ &- \tau(\cos^2\delta e^{-\tau/\cos\delta} - e^{-\tau}) \\ &+ \cos\delta(1+\cos(2\delta))e^{-\tau/\cos\delta} \\ &- 2e^{-\tau} + 2(1-\cos^3\delta)]\end{aligned} \quad (15)$$

where $\mathrm{Ei}(x)$ is the exponential integral:

$$\mathrm{Ei}(x) = \int_{-\infty}^{x}\frac{e^t}{t}dt, \quad (16)$$

$$\Sigma_2(\tau) = \frac{L_2}{L_1}\Sigma_1(\tau). \quad (17)$$

Equation (9) therefore gives:

$$\Sigma(\tau) = \left|\frac{\pi^2 - 2\beta^2 - \pi^2\cos\beta}{2(\pi^2-\beta^2)}\Sigma_1(\tau) - \frac{\pi^2\sin\beta}{2(\pi^2-\beta^2)}\Sigma_2(\tau)\right|. \quad (18)$$

The factor $\Lambda(\tau)$ in the last term gives:

$$\begin{aligned}\Lambda(\tau) &= \int_D (1 - e^{-\tau/|\cos\theta_0|})\sin\theta_0\,|\cos\theta_0|\,d\theta_0 \\ &= \frac{1}{2}[\tau^2(\mathrm{Ei}(-\tau) - \mathrm{Ei}(-\tau/\cos\delta)) \\ &\quad + \tau(e^{-\tau} - \cos\delta e^{-\tau/\cos\delta}) + (1-\cos^2\delta) \\ &\quad - (e^{-\tau} - \cos^2\delta e^{-\tau/\cos\delta})].\end{aligned} \quad (19)$$

For dielectric particles ($\omega = 0$) the multiple-scattering term in Equation (6) leads to

$$\begin{aligned}\chi(\tau) &= \int_D (1 - e^{-\tau/|\cos\theta_0|})^2\sin\theta_0\,|\cos\theta_0|\,d\theta_0 \\ &= \frac{1}{2}[4\tau^2(\mathrm{Ei}(-2\tau/\cos\delta) - \mathrm{Ei}(-2\tau)) \\ &\quad - 2\tau^2(\mathrm{Ei}(-\tau/\cos\delta) - \mathrm{Ei}(-\tau)) \\ &\quad + 2\tau(e^{-\tau} - \cos\delta e^{-\tau/\cos\delta}) \\ &\quad - 2\tau(e^{-2\tau} - \cos\delta e^{-2\tau/\cos\delta}) \\ &\quad - 2(e^{-\tau} - \cos^2\delta e^{-\tau/\cos\delta}) \\ &\quad + (e^{-2\tau} - \cos^2\delta e^{-2\tau/\cos\delta}) \\ &\quad + (1-\cos^2\delta)].\end{aligned} \quad (20)$$

For absorbing particles ($\omega \neq 0$) we have:

$$\begin{aligned}\chi(\tau) = \int_D & e^{-\tau(1-\omega)/|\cos\theta_0|}(1 - e^{-\tau\omega/|\cos\theta_0|}) \\ &\times (1 - e^{-\tau/|\cos\theta_0|})|\cos\theta_0|\sin\theta_0 d\theta_0 \\ = \frac{1}{4}[&-e^{-2\tau/\cos\delta} + e^{-\tau/\cos\delta} + e^{\tau(\omega-2)/\cos\delta} \\ &- e^{\tau(\omega-1)/\cos\delta} + 4\tau\cos\delta e^{-2\tau/\cos\delta} \\ &- 2\tau\cos\delta e^{-\tau/\cos\delta} - 4\tau\cos\delta e^{\tau(\omega-2)/\cos\delta} \\ &+ 2\tau\cos\delta e^{\tau(\omega-1)/\cos\delta} + 2\tau\omega\cos\delta e^{\tau(\omega-2)/\cos\delta} \\ &- 2\tau\omega\cos\delta e^{\tau(\omega-1)/\cos\delta} - \cos(2\delta)e^{-2\tau/\cos\delta} \\ &+ \cos(2\delta)e^{-\tau/\cos\delta} + \cos(2\delta)e^{\tau(\omega-2)/\cos\delta} \\ &- \cos(2\delta)e^{\tau(\omega-1)/\cos\delta} + 8\tau^2\mathrm{Ei}(-2\tau/\cos\delta) \\ &- 2\tau^2\mathrm{Ei}(-\tau/\cos\delta) - 8\tau^2\mathrm{Ei}(\tau(\omega-2)/\cos\delta) \\ &+ 8\tau^2\omega\mathrm{Ei}(\tau(\omega-2)/\cos\delta) \\ &- 2\tau^2\omega^2\mathrm{Ei}(\tau(\omega-2)/\cos\delta) \\ &+ 2\tau^2\mathrm{Ei}(\tau(\omega-1)/\cos\delta) \\ &- 4\tau^2\omega\mathrm{Ei}(\tau(\omega-1)/\cos\delta) \\ &+ 2\tau^2\omega^2\mathrm{Ei}(\tau(\omega-1)/\cos\delta)] \\ &- \frac{1}{2}[-e^{-2\tau} + e^{-\tau} + e^{\tau(\omega-2)} - e^{\tau(\omega-1)} + 2\tau e^{-2\tau} \\ &- \tau e^{-\tau} - 2\tau e^{\tau(\omega-2)} + \tau e^{\tau(\omega-1)} + \tau\omega e^{\tau(\omega-2)} \\ &- \tau\omega e^{\tau(\omega-1)} + 4\tau^2\mathrm{Ei}(-2\tau) - \tau^2\mathrm{Ei}(-\tau) \\ &- 4\tau^2\mathrm{Ei}(\tau(\omega-2)) + 4\tau^2\omega\mathrm{Ei}(\tau(\omega-2)) \\ &- \tau^2\omega^2\mathrm{Ei}(\tau(\omega-2)) + \tau^2\mathrm{Ei}(\tau(\omega-1)) \\ &- 2\tau^2\omega\mathrm{Ei}(\tau(\omega-1)) + \tau^2\omega^2\mathrm{Ei}(\tau(\omega-1))].\end{aligned} \quad (21)$$

Finally, the term V is simply obtained from the angular domain of illumination to be $1/2\sin^2\delta$. This completes the analytic integration of the general solution of Equation (6) for $I(\tau)$ in terms of the particle diameter, d, and the angular extent of the source, δ. By inserting $\beta = \frac{\pi}{b}$ and δ in $\Sigma(\tau)$, $\chi(\tau)$, $\Lambda(\tau)$ (Equations (18), (21), (19)), and K (Equation (8)) one obtains the analytic expression for $I(\tau)$ from Equation (3).

Below we compare the results of the analytic integrations leading to the expression for $\Sigma(\tau)$to the results obtained through numerical integration of the same functions. This allows us to illustrate the range of validity of the assumptions made to overcome the non-integrability in the expression leading to Σ_1. In Figure 4 the results are compared as a function of τ for various β. The accordance is good for $\beta > \frac{\pi}{6}$

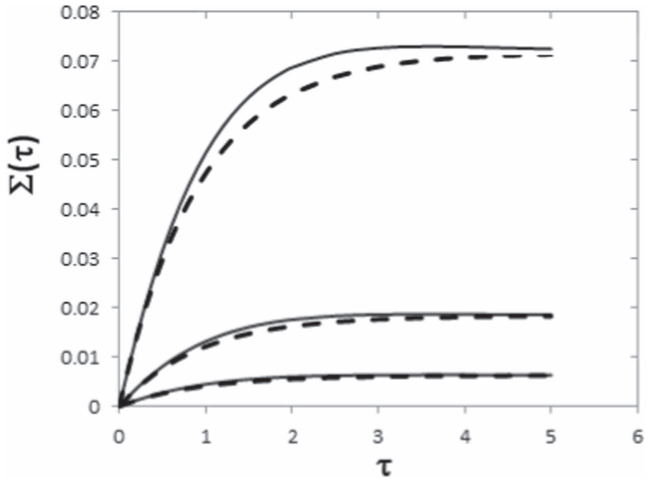

Figure 4. Comparison of the functions $\Sigma(\tau)$ in Equation (18) to the functions obtained through numerical integrations. Three β values are considered here: 0.25, 0.60, 1.66 rad, from top to bottom. The solid lines represent the analytic solutions, and the dashed lines represent the numerical approximations.

approximately. The highest discrepancy, about 10%, is at $\tau \approx 1$.

We also compared two transmission curves derived with the analytic expression obtained here using the simplified phase function and the numerical integration of Equation (3) with the correct phase function obtained from Mie theory. The results show that the analytic solution provides an excellent approximation to the extinction curve, with a maximum discrepancy of 2%.

The condition $\beta > \frac{\pi}{6}$ ultimately corresponds to $b < \frac{6\lambda}{\pi} \approx 2\lambda$. This assumption is fully consistent with the basic assumption of our model, which requires the particle to be small enough to make the light scattered twice (or more) be isotropic.

4. Experimental Validation

Even if our approximate solutions closely match the results of a rigorous treatment, given the number of assumptions we decided to compare our findings against real data. In this section we present the experimental apparatus we used to validate our results.

The setup is schematically sketched in Figure 5. A halogen lamp L (USHIO mod. EKE; power 150 W) illuminates a white diffuser acting as the source, *S*, composed by a 1 mm thick layer of titanium oxide deposited onto a glass surface, delimited by a circular diaphragm *D* (50 mm in diameter, or smaller). The optical axis is defined by the position of the source and the center of the diffuser; the diffuser is aligned perpendicular to the optical axis at a distance $z_0 = 56.5$ mm from the light source. A fraction of the diffused light impinges onto a cell, *C*, uniformly filled with a water suspension of particles, which represents the scatterer system undergoing the radiative transfer phenomena to be characterized. The cell is placed on a distance z from the diffuser, setting the solid angle Ω from which light illuminates the sample; by varying z we can obtain different illumination conditions. A second diaphragm, D_1 (2 mm in diameter), is placed just before the cell to prevent backscattered light to impinge onto the diffuser and then onto the cell again. Downstream from the cell, a couple of small diaphragms, D_2 and D_3 (2 mm in diameter), separated by a

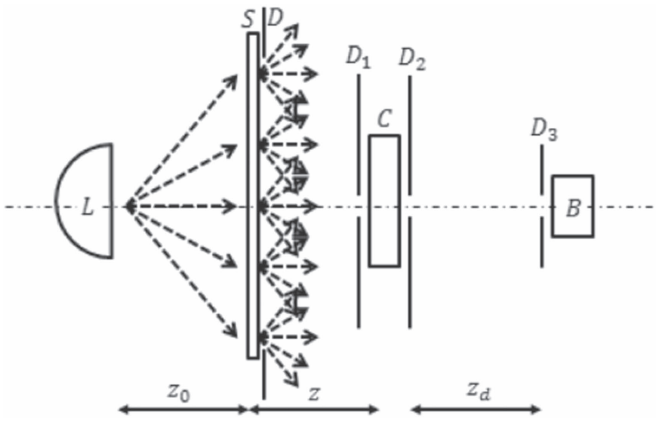

Figure 5. Schematic of the experimental apparatus. *L*: halogen lamp; *D*: large diaphragm; *S*: diffuser acting as the diffuse extended source; *C* sample cell; D_1, D_2, D_3: diaphragms; *B*: bolometer. The dashed arrows schematically represent the directions of the light rays emerging from the lamp and the diffuse source.

distance z_d, selects a very narrow set of directions just around the optical axis. A bolometer (mod. IF PM from *Industrial Fiber Optics*) measures the integrated power across the entire wavelength range.

Our methodology is as follows. First, the angular profile of the light directed toward the cell is measured to characterize the source. Then, by removing the diaphragm *D* and filling the cell with pure water, the bolometer is placed onto a goniometric rotation stage and an accurate characterization of the intensity passing through the cell is done. The results are represented in Figure 6.

In Figure 6 we present the intensity of the light emitted by the diffuser. By varying the distance between the diffuser and bolometer, we find that the light intensity is uniform within 5% up to an angle of 45°. Note the excellent reproducibility of the results for different distances (circles and triangles; see caption).

We must also take into account the spectral sensitivity of the sensor used in our measurements, which is reported in Figure 7,[5] and the spectral intensity of the illuminating lamp, a blackbody at temperature $T = 3000$ K (see above). Hereafter, we will refer to data corrected for both effects.

In the following sections we report the results obtained with $z = 44$ mm, corresponding to an angular aperture of the diffuse source of 21° in two cases: a suspension of calibrated particles and a set of non-homogeneous samples.

4.1. Transmission through Collections of Monodisperse, Calibrated Samples

In Figure 8 we present the results obtained using water suspensions of calibrated, monodisperse spherical latex particles. For these particles the whole set of parameters is well-known in terms of particle size, shape, composition, and concentration. Therefore, the radiative transfer model can be solved without any free parameter. Scattering properties have been evaluated with a consolidated code (Lompado 2002). We used the approximated value for the refractive index $n = 1.59$ over all the range of wavelengths. This is the average value of the refractive indexes within the spectral range we consider

[5] Datasheet available at http://i-fiberoptics.com/laser-accessories-detail.php?id=1018).

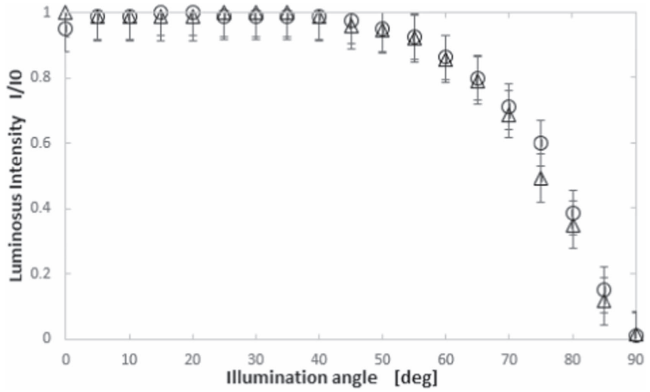

Figure 6. Angular dependence of the intensity emitted by the extended source and impinging onto the cell, measured at distances $z = 440$ mm (circles) and $z = 340$ mm (triangles).

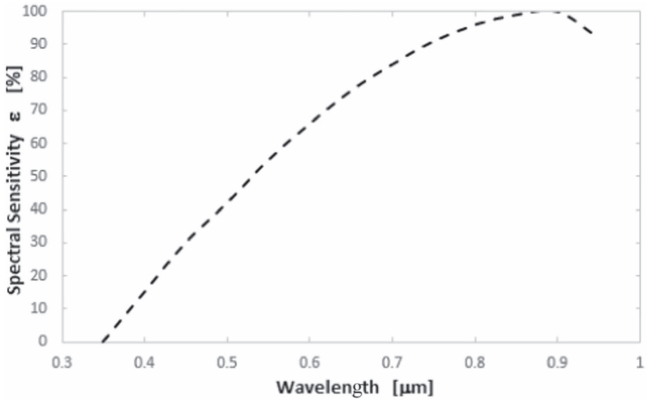

Figure 7. Spectral sensitivity ε of the bolometer.

here (Ma et al. 2003). Note that the change in refractive index is small, ranging from 1.61 (400 nm) to 1.575 (900 nm), while the imaginary part is negligible.

The radiative transfer in conditions of high optical thickness depends strongly on the angular source extension. Since in this case the light propagates in completely random directions, the solid angle subtended by the source determines the amount of light emerging in any given direction. Measurements were performed by changing the diameter of the diaphragm limiting the size of the source S, thus changing the angular aperture of the illuminating source; this provided results in agreement with Equation (5).

4.2. Polydisperse, Nonspherical Particles: Effects of Absorption

Here, we drop the assumptions of well-characterized monodisperse and spherical particles, moving to the study of fine powders with and without absorption. This covers all the cases of interest for interstellar grains. If the real part of n is large, the grain is an effective scatterer, which is the case for dielectric grains or icy grains.

If the imaginary part is large, the grain is an effective absorber, e.g., as is the case for metallic grains.

We have characterized each sample by performing independent ancillary measurements. As detailed in the Appendix, we used the following tools: (1) an optical turbidimeter, to measure the optical thickness; (2) absolute measurements of small-angle light-scattering, to get the angular phase function and the total

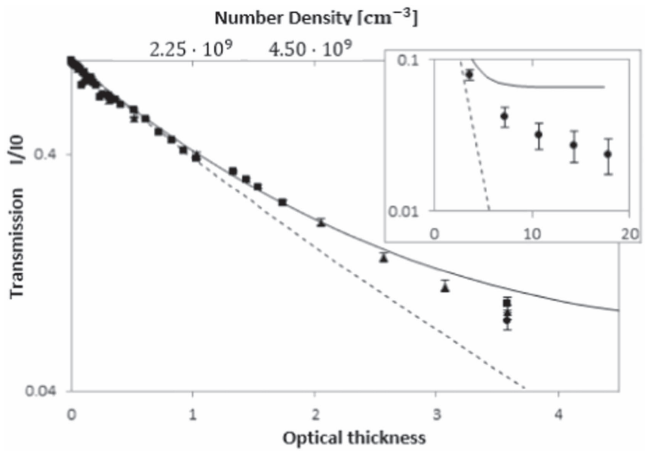

Figure 8. Experimental results obtained with calibrated, monodisperse polystyrene spheres. The dashed line represents the normalized transmission for collimated light without any multiply scattered component. The continuous line represents the result obtained with our model (without free parameters). In the inset the data obtained at the highest densities show a deviation from the results of the model.

scattering cross-section; and (3) spectrophotometry, to estimate the dependence of the parameters on the wavelength.

We performed a variety of measurements on two types of samples: (1) water suspensions of ceria oxide, composed of compact grains with negligible absorption, and (2) black carbon, which is endowed with high absorption at all wavelengths and has a very fluffy grain structure. Care has been taken to properly handle the samples to avoid sedimentation, aggregation, etc. Also, typical aggregation time constants have been evaluated and the measurements have been performed on the shortest possible timescale to reasonably exclude the formation of clusters. Independent checks have been done to verify the stability of the optical properties during the measurements.

In Figure 9(a) we plot the experimental results obtained for the normalized transmission through a suspension of ceria oxide at different concentrations. Samples have been prepared by diluting a suspension that is 5% concentrated by mass. The same sample has been accurately characterized as described in Potenza et al. (2015). Results are plotted versus the optical thickness obtained from the turbidimeter. The deviation from the collimated beam (dashed line) is similar to the previous case. Having measured all the optical properties necessary for modeling the radiative transfer, we obtain nice agreement between our model and the data without adjusting any free parameters.

In Figure 9(b) we plot the normalized transmission through a suspension of black carbon as a function of the optical thickness, evaluated again as described above. Suspensions of dry powder produced by Sennelier, one of the most famous dry pigments, have been used. They have been prepared by suspending dry powder in water, passing them through an ultrasound bath until the properties of the suspension stabilized (Sanvito 2013), and finally diluting them for the measurements. For the optical properties of this material we refer to Campbell et al. (1999) and Bergstrom & Bond (2006) and to direct measurements performed on the sample considered here (see the Appendix and Sanvito 2013). The deviation with respect to the collimated beam is smaller than that for dielectric particles, albeit non-negligible. Moreover, unlike the results plotted in

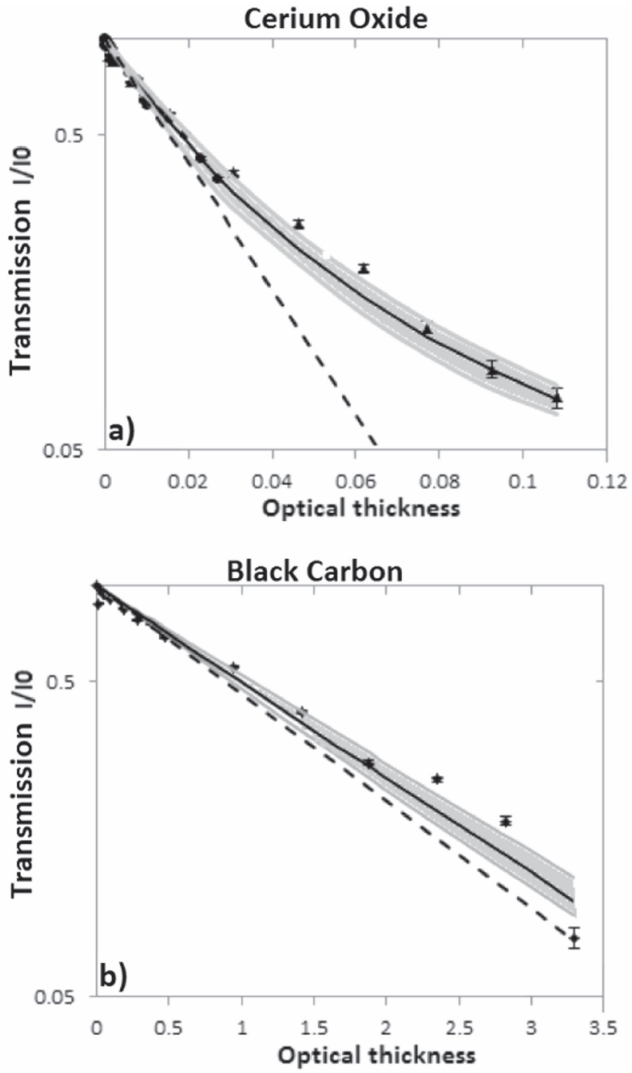

Figure 9. Experimental results obtained with suspensions of ceria oxide (a) and black carbon (b). The dashed line represents the normalized transmission for collimated light. The continuous line represents the result obtained with our model (without any free parameters). The region shown in gray indicates the uncertainty introduced in the model by exaggerating the uncertainties in the phase function.

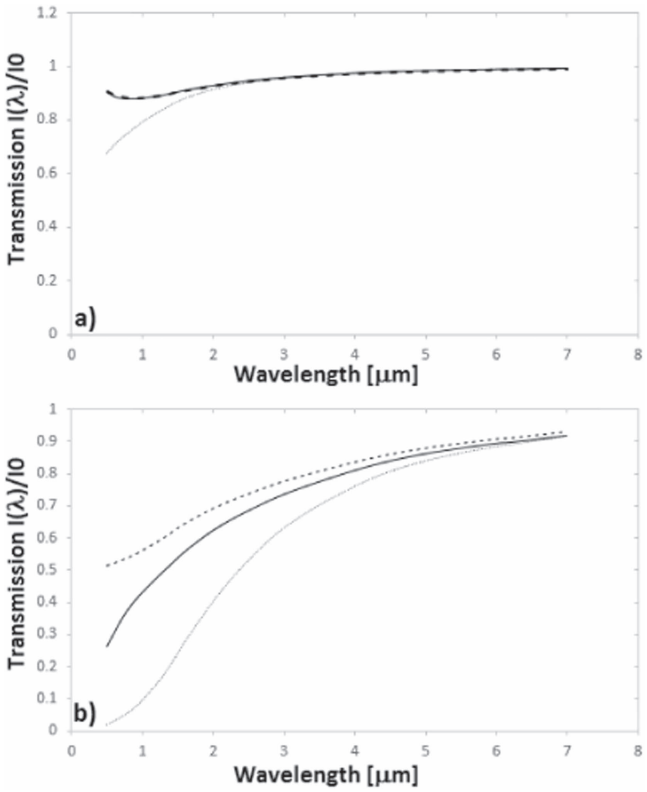

Figure 10. Diffuse transmission in the range 400 nm–8 μm through a cloud of interstellar dust as in Draine & Lee (1984), for an optically thin ($\tau = 0.5$ top panel) and optically thick ($\tau = 5$, bottom panel) case. The curves refer to the present method (solid lines), compared to the usual LBB model (dotted lines) and zero absorption (dashed lines) grains, treated with our method.

Figure 9, the asymptotic behavior at high optical thickness makes the transmission vanishingly small, as expected.

5. Application to Astronomical Grains

In this last section we discuss the effect of diffuse illumination on the spectral extinction when the cloud of particles has a composition and size distribution similar to those found in astrophysical cases. First, we consider the classic grains of Draine & Lee (1984), then a mixture of grains representative of protoplanetary disks, with a special application to the case of the giant dark silhouette disk 114–426 in Orion.

Draine & Lee (1984) provided a classic recipe for interstellar dust based on a combination of silicates and graphite. For our calculations we adopt the real and imaginary parts of the refractive index of their mixture. We assume a grain size distribution $n(a) \propto a^{-q}$, with a being the particle radius and q being the spectral index. We set $q = 3.5$ and a size range from $a_{\min} = 0.1$ μm to $a_{\min} = 0.5$ μm.

The top panel of Figure 10 shows the $\tau = 0.5$ case over the visible and IR wavelength range up to 8 μm. Large differences arise in the visible range, as the scattering efficiency, decreasing with wavelength, has a negligible effect in the IR. By contrast, in the visible, where the reduced size of the particle, $\beta = ka$, is close to unity, diffuse transmission is heavily affected by the presence of an extended background source, changing the reddening effect expected on the basis of the LBB law into an almost uniform transmission. For large optical thickness, $\tau = 5$ (bottom panel), the visible range is completely dominated by scattered light, and the wavelength dependence of the transmitted light (appearing as reddening) is appreciably shifted to shorter wavelengths with respect to the LBB model. In this case the presence of an extended source affects the reddening curve even in the IR region, and the transmission remains generally higher with respect to the LBB law.

For protoplanetary disk grains, we use the set of refraction indexes provided by Ricci et al. (2010) and the grain composition adopted in Pollack et al. (1994; 30% vacuum, 21% carbonaceous, 7% astronomical silicates, 42% water ice). We maintain the size distribution $n(a) \propto a^{-3.5}$ adopted for the Draine & Lee (1984) grains. By evaluating the complex dielectric functions for each material from the tabulated refractive indexes, and using the mean field approximation for the composite grains (Bohren & Huffman 1998), we obtain the grain refractive index as a function of wavelength λ.

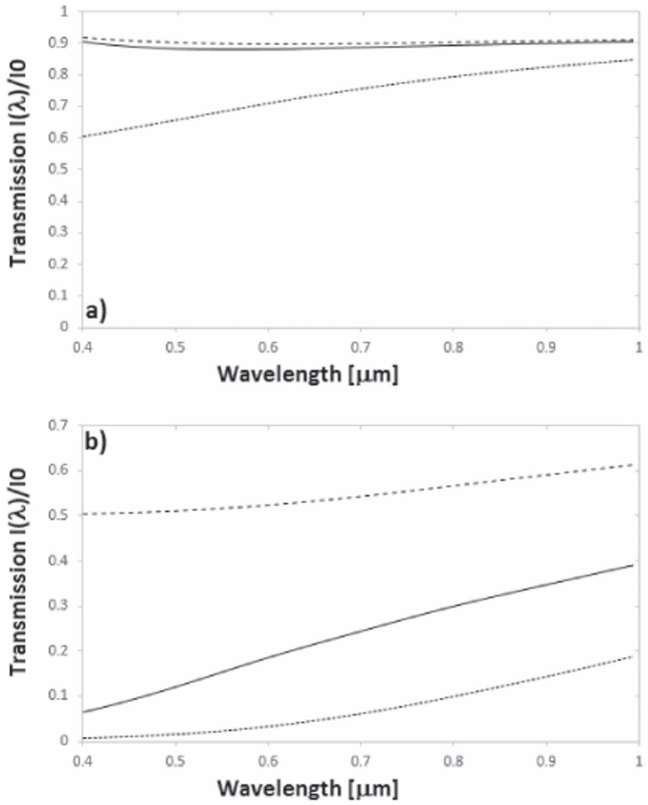

Figure 11. Similar to Figure 10 for grains typical of protoplanetary disks, according to Ricci et al. (2010), in the wavelength range 400–1000 nm. Solid lines: our model with uniform background illumination; dotted lines: LBB model; dashed lines: dielectric (zero absorption) grains treated with our model.

If we assume the particles to be spherical, a reasonable approximation in our case as discussed by Pollack et al. (1994), we can use the analytic approach described earlier by adopting the reduced size of the scatterers (scattering form factor) $\beta(\lambda) = 2\pi a/\lambda$. For the sake of simplicity, the size range is divided into 5 bins, 0.1 μm-wide each, and the optical properties calculated for the corresponding size values a_i, $i = 1,\ldots,5$. In order to maintain the analytic approach presented so far, we adopt an approximate expression for evaluating the cross-section and the single-scattering albedo following Van de Hulst (1981; chapter 2); analytic expressions for the extinction and absorption cross-sections allow us to derive the scattering term.

According to the notation used in Van de Hulst (1981); the refractive index is described as $m = n - in'$), we obtain the scattering albedo and optical thickness in terms of the absorption and extinction *efficiency factors*:

$$Q_{\rm ext}(a,\,\lambda) = \frac{C_{\rm ext}}{\pi a^2} = 4\,{\rm Re}[K(i\rho + \rho\tan\gamma)]$$
$$Q_{\rm abs}(a,\,\lambda) = \frac{C_{\rm abs}}{\pi a^2} = 2K(4\beta n'), \qquad (22)$$

where $\rho = 2\beta(n-1)$ and $\tan\gamma = \frac{n'}{n-1}$ and

$$K(z) = \frac{1}{2} + \frac{e^{-z}}{z} + \frac{e^{-z}-1}{z^2}. \qquad (23)$$

We obtain the scattering albedo as

$$\omega(a,\,\lambda) = 1 - \frac{Q_{\rm abs}(a,\,\lambda)}{Q_{\rm ext}(a,\,\lambda)}. \qquad (24)$$

The approximations leading to Equation (22) are valid for the goal of this case study, as we are aiming at a quantitative comparison of the diffuse transmission calculated with our model against the basic LBB expectations. Higher accuracy can be achieved by introducing the full Mie expansions. With these elements, the extinction ratio of the cloud $r = I/I_0$ is obtained as a function of wavelength λ. Here we assumed the cloud to be illuminated from the full hemisphere opposite to the observer ($\delta = \pi/2$).

Figure 11 shows the diffuse transmission estimated using our model for a cloud of dust composed by a mixture of silicates, carbonaceous grains, ice, and vacuum as described in Ricci et al. (2010) for two values of the cloud optical thickness, $\tau = 0.5$ (top panel) and $\tau = 5$ (bottom panel). For clarity, we are referring here to the maximum value of τ over the considered wavelength range. The effect of the diffuse illumination of the cloud is evident, giving rise to appreciable changes in the shape of the transmission spectrum. When $\tau = 0.5$, the departure from the LBB law makes the extinction nearly the wavelength. When $\tau = 5$, the wavelength dependence originates a reddening law appreciably different from the one resulting from the LBB treatment. The influence of absorption is also evident. Note that for $\tau = 5$ the light intensity is mainly due to light from the diffuse source, which is scattered toward the observer.

The top panel shows that in the optically thin case there are clear differences between the reddening effect expected on the basis of the LBB law (dotted line) and the nearly uniform extinction predicted by our model (solid line). The dashed line represents the result obtained by artificially forcing the absorption to zero: the effect of absorption is negligible. The bottom panel shows how things change in the optically thick case. Over the visible spectrum most of the light comes from scattering instead of being passed undisturbed through the cloud, as evidenced by the negligible values obtained for the LBB model at the shortest wavelengths compared to the finite intensity obtained with our model. The presence of scattering increases the measured transmission with respect to the LBB law, but the reddening effect is present in both cases. If we artificially set the absorption to zero, reddening becomes negligible as the light coming from the diffuse source is dominated by scattering. This case of non-absorbing material, although slightly unphysical here, warrants a final remark. For a cloud with large optical thickness with no absorption, isotropic scattering guarantees that half of the total amount of light emerges toward the observer. This is in accordance with the limit case we discussed in Section 2.

Finally, to assess how the application of our model may affect the interpretation of real astronomical data, we apply our treatment to the outer regions of the 114–426 protoplanetary disk in Orion, previously analyzed by Miotello et al. (2012) in the framework of the standard LBB extinction law. The composition of the protoplanetary disk grains discussed above is identical to the one used by Miotello et al. (2012). It is therefore sufficient to adopt the same value of Miotello et al. (2012) for the intensity of the illuminating source, assumed this time to be uniform over a 2π hemisphere, to immediately

Table 1
Comparison of the Results Obtained with the Classical LBB Law by Miotello et al. (2012) and Our Model (Indicated Here as the Radiative Transfer Model, RTM) for (a) the Typical Radius of the Dust Grains (Columns 1 and 2); (b) the Product nL between the Number Density n and the Geometrical Thickness of the Scattering Column L (Columns 3 and 4); and (c) the Optical Thickness

	$a(\mu\mathrm{m})$		$nL(\mu\mathrm{m}^{-2})$		$\tau_{0.55}$	
	LBB	RTM	LBB	RTM	LBB	RTM
Pixel A	0.6	0.6	0.59	1.71	0.98	5.28
Pixel B	0.5	0.5	0.55	1.45	0.95	3.28
Pixel C	0.4	0.5	0.83	1.12	0.73	2.00

derive and compare the values obtained for the average grain size and optical depth.

We refer in particular to the three pixels A, B, C, of Miotello et al. (2012), located at the northeast edge of the disk. The results shown in Table 1 are relative to (a) the average grain size; (b) the product of the grain number density n times the geometric thickness L of the region, in units of $\mu\mathrm{m}^{-2}$, which is the wavelength-independent parameter directly returned by our model fitting, together with the grain radius a; and (c) the adimensional optical thickness, given by the product $nL\sigma_g$.

Table 1 shows that the two methods return about the same average grain size, $a \simeq 0.5\ \mu\mathrm{m}$. The other values, however, are significantly different. In particular, the product nL, which basically represents the number of particles that have contributed to the observed extinction, increases by a factor $\simeq 1.3 - 2.9$, whereas the optical thickness at 0.55 μm increases from $\tau \lesssim 1$ to $\tau = 5.26, 3.28, 2.00$ for pixels A, B, C, respectively. Accounting for the extended background illumination makes the spectral energy distribution emitted by the outer disk regions compatible with an optically thick medium. The column density estimated using the LBB law may therefore represent a lower limit.

It must be remarked that in this specific case the outer disk regions may lie in the shadow of the thick disk, i.e., the illumination from the background may mostly come from less than 2π sr. We have detected some indication of this "edge effect" in our experimental setup. Also, the emitting columns subtended by the 3 pixels may not be well represented by the uniform plane-parallel slab we have assumed. Accounting for these effects would require a more refined treatment of the geometry of the outer disk regions, which is still uncertain and beyond the scope of this work.

6. Conclusions

In this paper we have revisited the RTE theory for clouds of scatterers illuminated by an extended background source. We have derived a rigorous solution based on the assumption that multiple-scattering produces an isotropic flux. We have then derived an approximate analytic model that nicely matches the results of the rigorous approach, and compared our predictions with accurate measurements for various types of well-characterized scatterers, finding an excellent match without the need of adding free parameters.

We have used the predictions of our model to explore the behavior of an astrophysical cloud with dust grains having parameters, in terms of size distribution, composition, and optical properties, that are typical of interstellar disks and the classic ISM grains of Draine & Lee (1984), illuminated by a diffuse source. We find that the clouds still exhibit properties of reddening, as expected on the basis of the LBB law, but they are appreciably modified in terms of the transmission and shape of the spectral intensity distribution. In particular, for small optical thickness our results show that scattering makes reddening negligible at visible wavelengths. Once the optical thickness increases enough and the probability of scattering events becomes close to or larger than 1, reddening is appreciably modified by the amount of radiation coming from directions different from the line of sight and scattered toward the observer. Moreover, variations of the grain refractive index, in particular the amount of absorption, play an important role in changing the shape of the spectral transmission curve, with dielectric grains showing the minimum amount of reddening. The results presented in this work could also be useful for studying the atmospheres of extrasolar planets and brown dwarfs, where the presence of non-isotropic phase functions is the issue currently limiting analytic solutions of RTE (Bailey 2014).

The authors wish to acknowledge L. Ricci and W. Henney for early discussions on the radiative transfer through dark silhouette disks in the Orion Nebula. They are also indebted to the anonymous referee for careful review of the original manuscript and helpful comments.

Appendix

Here, we briefly present the methods we adopted to determine the quantities needed for the model to be compared to the results obtained with nonspherical particles, namely ceria oxide and black carbon.

We performed measurements with a commercial spectrophotometer (SP), a custom laser turbidimeter (LT), a small-angle laser light-scattering (SALS) based upon the novel method of near-field scattering (Mazzoni et al. 2013), and a custom optical particle counter. Thanks to these independent measurements, the scattering-phase functions $p(\mu)$, the scattering-optical depths τ_{sca}, and the extinction-optical depth τ_{ext} have been determined as a function of the wavelength as described below, thus completing the parameters needed to evaluate the extinction curve accordingly to our model.

The parameters have been determined as follows. The spectrophotometer provided the extinction of the sample as a function of the wavelength, $\tau_{\mathrm{sca}}(\lambda)$. The same samples have also been measured with the LT for giving an absolute, precise check of the extinction efficiency measured with the SP at the wavelength of the laser ($\lambda_0 = 632.8$ nm). We adopted this additional check to be sure that the SP measurement was absolutely not affected by contributions coming from multiple-scattering events. This contribution is rigorously gotten rid of with the LT, while in principle it could be still present in the SP, especially for the ceria oxide suspension (when the extinction is almost completely due to scattering with no absorption).

We then measured the samples with SALS covering a scattering wavevector range from 0.1 to 4 $\mu\mathrm{m}^{-1}$. This range corresponds to an angular range wide enough to include almost the whole scattering lobe for both of the samples, and thus allowing the determination of the phase functions $p(\mu)$. Moreover, the SALS measurements also provide an absolute measurement of the total scattering cross-section, which immediately leads to $\tau_{\mathrm{sca}}(\lambda_0)$ at the laser wavelength. In the

case of the ceria oxide this result is in accordance with the value measured with the SP (and the LT, which operates at a very similar wavelength of SALS), meaning that $\tau_{\rm sca}(\lambda_0) = \tau_{\rm ext}(\lambda_0)$ and $\tau_{\rm abs}(\lambda_0) = 0$. By contrast, black carbon provided $\tau_{\rm sca}(\lambda_0) < \tau_{\rm ext}(\lambda_0)$, so $\tau_{\rm abs}(\lambda_0) > 0$ in accordance with the absorbing nature of the material.

Now we introduce a simple assumption for evaluating the spectral albedos: both ceria oxide and black carbon are endowed with uniform albedos over all the wavelength spectrum, according to their white and black colors. As a result, it is now possible to estimate the $\tau_{\rm sca}(\lambda)$ as follows:

$$\tau_{\rm sca}(\lambda) = \tau_{\rm ext}(\lambda)\frac{\tau_{\rm sca}(\lambda_0)}{\tau_{\rm ext}(\lambda_0)}, \quad (25)$$

and therefore $\tau_{\rm abs}(\lambda) = \tau_{\rm ext}(\lambda) - \tau_{\rm sca}(\lambda)$, in such a way that the extinction curve provided by our model can be evaluated without any free parameter, as has been shown in the main text (see Figure 9).

References

Alves, J. F., Lada, C. J., & Lada, E. A. 2001, Natur, 409, 159
Bailey, J. 2014, PASA, 31, e043
Barman, S. K. 2000, JQSRT, 66, 509
Bergstrom, R., & Bond, T. C. 2006, AerST, 40, 27
Biganzoli, D. 2014, Masters thesis, Univ. Milano
Bohren, C. F., & Huffman, D. R. 1998, Absorption and Scattering of Light by Small Particles (Berlin: Wiley-VCH)
Campbell, D., Bond, T. C., & Anderson, T. L. 1999, AerST, 30, 582
Chalhoub, E. S. 2005, JQSRT, 92, 335
Chandrasekhar, S. 1960, Radiative Transfer (New York: Dover)
Davidovic, D. M., Vukanic, J., & Aresnovic, D. 2008, Icar, 194, 389
Draine, B. T., & Lee, H. M. 1984, ApJ, 285, 89
Dunham, M. M., Stutz, A. M., Allen, L. E., et al. 2014, in Protostars and Planets VI, ed. B. Henrik et al. (Tucson, AZ: Univ. Arizona Press)
Flagey, N., Goldsmith, P. F., Lis, D. C., et al. 2013, ApJ, 762, 11
Herman, B. M., & Browning, S. R. 1965, JAtS, 22, 559
Ingalls, J. G., Bania, T. M., Boulanger, F., et al. 2011, ApJ, 743, 174
Jablonski, A. 2012, CoPhC, 183, 01773
Liuo, K. 1973, JAtS, 30, 1303
Lompado, A. 2002, Mathematica Version 4.2, Light Scattering by a Spherical Particle (Univ. Alabama)
Ma, X., Lu, Y. Q., Brock, R. S., et al. 2003, PMB, 48, 4165
Mazzoni, S., Potenza, M. A. C., Alaimo, M. D., et al. 2013, RScI, 84, 043704
Miotello, A., Robberto, M., Potenza, M. A. C., & Ricci, L. 2012, ApJ, 757, 78
Plass, G. N., Kattawar, G. W., & Catchings, F. E. 1973, ApOpt, 12, 314
Pollack, J. B, Hollenbach, D., Beckwith, S., et al. 1994, ApJ, 421, 615P
Potenza, M. A. C., Sanvito, T., & Pulliam, A. 2015, JNR, 17, 110
Purcell, E. M., & Pennypacker, C. R. 1973, ApJ, 186, 705
Ricci, L., Testi, L., Natta, A., Neri, R., Cabrit, S., & Herczeg, G. J. 2010, A&A, 512, A15
Sanvito, T. 2013, PhD thesis, Univ. Milan
Shuping, R. Y., Bally, J., Morris, M., & Throop, H. 2003, ApJL, 537, L109
Siewert, C. E. 2000, JQSRT, 64, 109
Taflove, A., Umashankar, K. R., Beker, B., Harfoush, F. A., & Yee, K. S. 1988, IEEE Transactions on Antennas and Propagation, 36, 247
Tanaka, T. 2003, JQSRT, 76, 121
Tanaka, T. 2005, JQSRT, 95, 71
Van de Hulst, H. C. 1981, Light Scattering by Small Particles (New York: Dover)
Van Dishoeck, E. F., & Black, J. H. 1986, ApJS, 62, 109